Sea spray aerosol concentration modulated by sea surface temperature

Shang Liu[a,b,1,2,3], Cheng-Cheng Liu[c,1], Karl D. Froyd[a,b], Gregory P. Schill[a,b], Daniel M. Murphy[b], T. Paul Bui[d], Jonathan M. Dean-Day[e], Bernadett Weinzierl[f], Maximilian Dollner[f], Glenn S. Diskin[g], Gao Chen[g], and Ru-Shan Gao[b]

[a]Cooperative Institute for Research in Environmental Sciences, University of Colorado, Boulder, CO 80309; [b]NOAA Chemical Sciences Laboratory, Boulder, CO 80305; [c]School of Earth and Space Sciences, University of Science and Technology of China, Hefei, Anhui 230026, China; [d]Atmospheric Science Branch, NASA Ames Research Center, Moffett Field, CA 94035; [e]Bay Area Environmental Research Institute, Moffett Field, CA 94035; [f]University of Vienna, Faculty of Physics, Aerosol Physics and Environmental Physics, 1090 Vienna, Austria; and [g]Chemistry and Dynamics Branch, Science Directorate, NASA Langley Research Center, Hampton, VA 23681

Edited by John H. Seinfeld, California Institute of Technology, Pasadena, CA, and approved December 29, 2020 (received for review October 1, 2020)

Natural aerosols in pristine regions form the baseline used to evaluate the impact of anthropogenic aerosols on climate. Sea spray aerosol (SSA) is a major component of natural aerosols. Despite its importance, the abundance of SSA is poorly constrained. It is generally accepted that wind-driven wave breaking is the principle governing SSA production. This mechanism alone, however, is insufficient to explain the variability of SSA concentration at given wind speed. The role of other parameters, such as sea surface temperature (SST), remains controversial. Here, we show that higher SST promotes SSA mass generation at a wide range of wind speed levels over the remote Pacific and Atlantic Oceans, in addition to demonstrating the wind-driven SSA production mechanism. The results are from a global scale dataset of airborne SSA measurements at 150 to 200 m above the ocean surface during the NASA Atmospheric Tomography Mission. Statistical analysis suggests that accounting for SST greatly enhances the predictability of the observed SSA concentration compared to using wind speed alone. Our results support implementing SST into SSA source functions in global models to better understand the atmospheric burdens of SSA.

marine aerosols | sea surface temperature | wind speed | NASA ATom

Over two-thirds of the Earth is covered by the ocean. The material exchange between the ocean and the atmosphere affects the balance of the Earth's energy on a global scale (1). Sea spray aerosol (SSA) is the major particulate material directly emitted from the ocean. Studies have shown that SSA dominates the aerosol mass in the marine boundary layer (MBL). Such dominance renders SSA an important player in climate change (2). However, the exact processes by which the SSA is introduced to the atmosphere still remains to be learned, making the SSA budget highly uncertain (3).

It is generally established that SSA is produced by mechanical processes (4–6). Wind stress induces breaking waves that entrain bubbles into the surface ocean (7). Film and jet drops formed during bubble bursting are the main sources of SSA particles (8). The wind-driven mechanism is supported by the positive correlation between wind speed and SSA concentration from field observations (9, 10). Therefore, wind speed is used as the sole parameter to characterize SSA in many models (1, 4, 11).

In addition to wind speed, sea surface temperature (SST) may play a large role in SSA production (12–15). SST affects the drop formation process by modifying the physical properties of the surface ocean water. An increase of SST reduces the kinematic viscosity and surface tension of the ocean, thereby enhancing the entrainment efficiency and rising speed of bubbles (12, 16). As a result, the number size distribution of the bubbles may change, leading to varying SSA properties (14, 15, 17).

Limited laboratory and field studies regarding the effects of SST on SSA production have shown disparate results. Some argue that SSA production is independent of SST (18) or suppressed by increasing SST (14, 15, 19, 20) from 0 to 10 °C, while other laboratory (12, 21–23) and field measurements (3, 5) suggest that SSA production increases monotonically with water temperature. Furthermore, recent observations in the remote Atlantic Ocean shows that increasing SST enhances the modal mean diameter of SSA (24). On the other hand, model simulations have demonstrated that incorporating SST into SSA source functions generally improves the SSA prediction (3, 25, 26). The inconsistency in the previous work suggests that the impacts of SST on SSA formation remain unclear.

In this study, we conducted unprecedented aircraft measurements of SSA concentration on a global scale during the Atmospheric Tomography Mission (ATom). These measurements consist of a series of flights spanning three seasons (summer, fall, and winter) over remote oceans (Fig. 1 and *SI Appendix*, Fig. S1). Our observations again confirm that wind speed is the dominant factor controlling the concentration of SSA. Further, we show that increasing SST enhances the mass concentration of SSA.

Significance

Climate models use pre-industrial atmosphere as the reference to evaluate the impacts of human activities on the Earth's radiation balance. Sea spray aerosols (SSA) are the key component in the relatively pristine preindustrial conditions that substantially affect model calculations. Currently, the abundance of SSA is poorly constrained. In particular, studies on the influence of sea surface temperature on SSA production have shown disparate results. This uncertainty arises from limited field measurements, especially over remote oceans. Our global aircraft measurements over the remote Pacific and Atlantic Oceans show that higher sea surface temperature enhances the production of SSA. Updating the current parameterization in global models using our observational constraints will improve the estimate of atmospheric SSA budget and human-induced climate change.

Author contributions: R.-S.G. designed research; S.L., K.D.F., G.P.S., D.M.M., T.P.B., J.M.D.-D., B.W., M.D., G.S.D., and R.-S.G. performed research; S.L. and R.-S.G. contributed new reagents/analytic tools; S.L., C.-C.L., K.D.F., G.P.S., D.M.M., T.P.B., B.W., M.D., G.S.D., and G.C. analyzed data; and S.L. and C.-C.L. wrote the paper.

The authors declare no competing interest.

This article is a PNAS Direct Submission.

[1]S.L. and C.-C.L. contributed equally to this work.

[2]Present address: Research Division, California Air Resources Board, Sacramento, CA 95814.

[3]To whom correspondence may be addressed. Email: shangliu2012@gmail.com.

This article contains supporting information online at https://www.pnas.org/lookup/suppl/doi:10.1073/pnas.2020583118/-/DCSupplemental.

Published February 22, 2021.

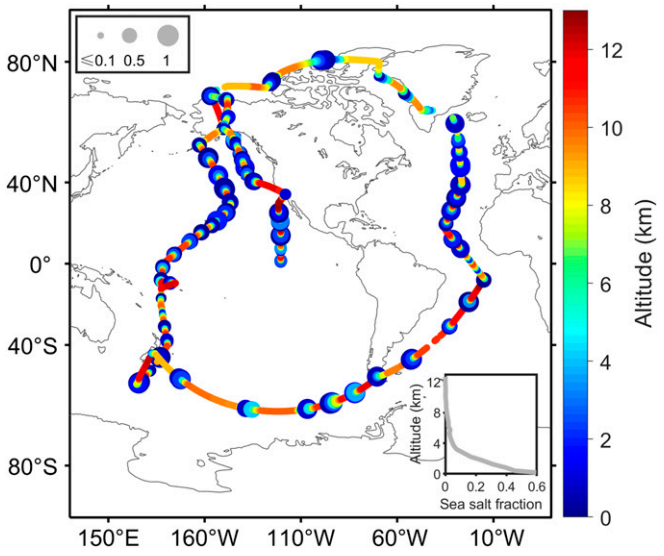

Fig. 1. Flight tracks during ATom2. The color indicates the flight altitude. The size of the markers represents the sea salt number fraction. The inset in the bottom right shows the vertical profile of sea salt number fraction. The flight tracks during ATom3 and ATom4 are similar to ATom2.

Results and Discussion

We measured the aerosol size distributions in the size range of 0.2 to 3 μm using an optical particle counter (the portable optical particle spectrometer [POPS] instrument) with a one second time resolution. In the meanwhile, we measured aerosol chemical composition with single-particle mass spectrometry (the particle analysis by laser mass spectrometry [PALMS] instrument), from which sea salt number fraction was derived. Combining the POPS and PALMS measurements, the volume fraction of sea salt was estimated at 1-min intervals (*Materials and Methods*). To ensure data quality, we performed a series of data screening procedures (*Materials and Methods*). In particular, particles smaller than 0.5 μm were excluded as they likely have nonmarine sources (27). Particles larger than 0.5 μm were predominately sea salt with an average sea salt volume fraction of 0.9. In this work, we used the POPS-measured aerosol particles (0.5 to 3 μm) as a proxy of SSA for the in-depth analysis.

SSA Concentration versus Wind Speed. The abundance of SSA decreased sharply with increasing altitude (Fig. 1). We focused our analysis on the measurements closest to the ocean surface, that is, the flight data collected in the 150 to 200 m altitude (above sea level [a.s.l.]) where the average number and volume fraction of sea salt was 0.6 and 0.9, respectively. Aerosol measurements in this range represent marine aerosols mixed into the MBL after production. The observed SSA size distribution is representative of typical SSA. The SSA volume size distribution (*SI Appendix*, Fig. S2 *D–F*) showed a peak at 2.2 μm, which is comparable to previous field measurements of SSA in the MBL (28). The measured wind speed at 150 to 200 m height (a.s.l.) compared well with wind speed at 10 m (a.s.l.) from the ERA5 reanalysis (*SI Appendix*, Fig. S3). This suggests that the 150 to 200-m height wind speed can be used as a proxy for near-surface wind speed (29), which is usually applied in the source functions for SSA generation (11).

Our global measurements provide robust evidence for the wind-driven SSA production mechanism. We observed a strong, positive correlation between horizontal wind speed (WS_h) and the SSA volume (Fig. 2 and *SI Appendix*, Figs. S4 and S5), with their r values of 0.90, 0.88, and 0.79 for all data during ATom2, ATom3, and ATom4, respectively. Measurements over individual oceans showed enhanced SSA volume as a function of increasing WS_h with variable dependencies (*SI Appendix*, Table S1). In general, wind speed has a stronger influence on supermicron particles (Fig. 2*B* and *SI Appendix*, Fig. S4 *C* and *D*). The correlation of instant wind speed with SSA concentration suggests that the SSA is strongly influenced by local production and have a relatively short lifetime. Since particle dry deposition is an increasing function of wind speed (30), the enhancement of SSA concentration at higher wind speed could be larger if the effect of dry deposition was removed.

The wind speed–SSA relationship was supported by aerosol composition measurement. Greater sea salt number fraction was associated with higher WS_h (Fig. 2 and *SI Appendix*, Fig. S4), consistent with the dominant role of wind speed in the production of SSA. In addition, our observed dependence of SSA on wind speed falls within the range of SSA–wind speed relationship reported by previous studies (*SI Appendix*, Fig. S6).

SSA Concentration Modulated by SST. Although wind speed can explain more than half of the variability of the observed SSA, substantial scatters exist for the WS_h versus SSA relationship (Fig. 2*A* and *SI Appendix*, Fig. S4). The residual, the difference between the observed SSA and the calculated SSA using WS_h (linear regression in Fig. 2*A* and *SI Appendix*, Fig. S4), exhibited a positive dependence on SST for all ATom campaigns (Fig. 3 and *SI Appendix*, Fig. S7). The result suggests that predicting SSA using wind speed alone underestimates the SSA in warm

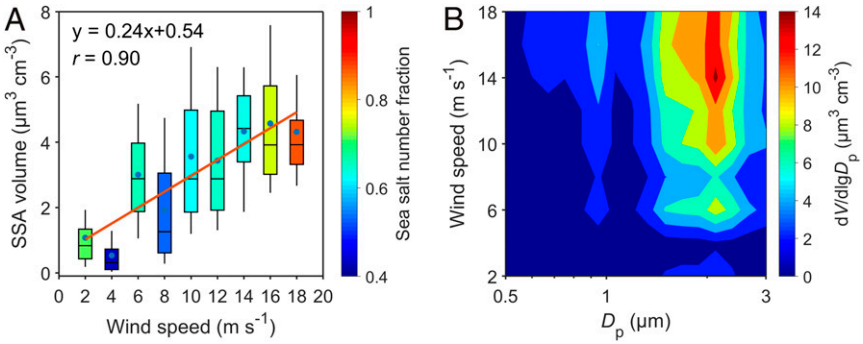

Fig. 2. SSA volume versus wind speed. (*A*) SSA volume concentration versus WS_h, colored by sea salt number fraction during ATom2. The box edges represent 25th and 75th quantiles. The whiskers represent 10th and 90th quantiles. The horizontal bars in the boxes denote median values. The blue dots indicate mean values. The red line is the linear regression for the mean values, with the equation and correlation coefficient r value shown in the legend. The mean sea salt number fraction was 0.73, 0.45, 0.67, 0.54, 0.64, 0.67, 0.65, 0.77, and 0.88 for each box, respectively. (*B*) The relationship of SSA volume size distribution and wind speed during ATom2.

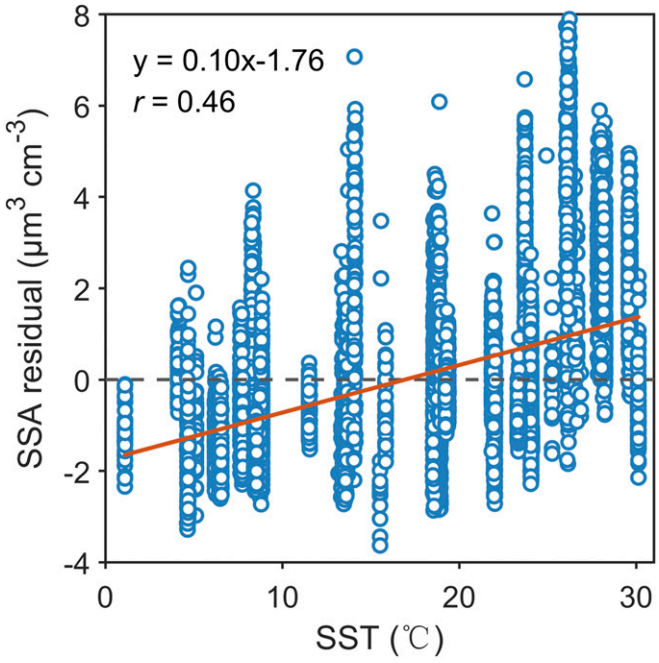

Fig. 3. SSA residual as a function of SST. The residual was derived as the difference between the observed SSA and the calculated SSA using the linear regression in Fig. 2*A* during ATom2. The red line represents the linear regression, with the equation and *r* value shown in the legend.

waters and overestimates SSA in cold waters, providing additional observational evidence for a previous study using global chemical transport model compared to surface and remote sensing observations (3).

To explore how SST affects SSA, we studied the relationship between SSA and SST in WS_h bins, in which the wind speed was relatively constant. This would largely remove the influence of wind speed on SSA. We observed a positive correlation between SSA volume and SST for the wind speed of 5 to 20 $m \cdot s^{-1}$ for ATom2 through 4 (Fig. 4 and *SI Appendix*, Figs. S8 and S9). The ATom2 had sufficient data that allow a comparison of linear regression slopes across wind speed intervals. The slope values for SSA versus SST were 0, 0.13, 0.11, and 0.19 $\mu m^3\ cm^{-3} \cdot °C^{-1}$ for wind speed bins of 0 to 5, 5 to 10, 10 to 15, and 15 to 20 $m \cdot s^{-1}$, respectively (Fig. 4), suggesting that SSA concentration is likely more sensitive to SST at higher wind speed. Furthermore, for the wind speed of 5 to 10 $m \cdot s^{-1}$, where ample SST data exist during ATom, we observed that SST has a stronger influence on the larger SSA particles (*SI Appendix*, Fig. S10).

Our global measurement is consistent with the laboratory studies that show a monotonic increase of SSA production as a function of increasing SST for ~0 to 30 °C (12). The suppression of SSA production for lower SST (0 to 10 °C) as indicated by some laboratory simulations (14, 15, 19) was not observed from the ATom campaigns (*SI Appendix*, Table S2).

The results from this study support previous field observations, most of which suggest that SST enhances the SSA concentration (*SI Appendix*, Table S2). The slope values of normalized SSA concentration ($[SSA]_{norm}$) versus SST for wind speed at 5 to 10 $m \cdot s^{-1}$ (10-m wind speed from ERA5) were 0.040, 0.064, and 0.048 $°C^{-1}$ during ATom2, ATom3, and ATom4, respectively. These values are comparable to the $[SSA]_{norm}$ versus SST slope value of 0.031 $°C^{-1}$ derived from the multiyear measurements using station networks and cruise ships at the same wind speed range (5) (*SI Appendix*, Fig. S11*B*). Cruise measurement during the International Chemistry Experiment in the Arctic LOwer Troposphere campaign (9) shows that the linear dependence of [Na] (in supermicron particles) on wind speed has a slope ~5 times larger in the North Atlantic compared to that in the Arctic. This result indicates that SST could enhance the SSA concentration at the same wind speed, which is consistent with our observation. Recent cruise measurements (24) show that SSA versus SST has a slope of 0.15 $\mu g\ m^{-3} \cdot °C^{-1}$. This value is in the range of the SSA versus SST slopes (0.08 to 0.50 $\mu g\ m^{-3} \cdot °C^{-1}$) at 5 to 10 $m \cdot s^{-1}$ wind speed for the overall and individual oceans during the ATom campaigns (*SI Appendix*, Fig. S11*A* and Table S3). Our study also complements the shipboard measurements in the North Atlantic (24), in which SST is shown to enhance the mode diameter of SSAs number size distribution. Together, these field measurements are consistent with the hypothesis that SST enhances the concentration of SSA.

Influence of SST on SSA Production. The SSA concentration is the net result of production and removal, both of which can be related to SST. Here we discuss how the removal processes could affect the SSA concentration. This analysis allows us to bridge SST and SSA production. The removal processes can be categorized into dry deposition and wet deposition. For a given particle size, the rate of dry deposition increases with increasing wind speed (30). This effect was accounted for in the SSA residual versus SST relationship when the effect of wind speed was removed. Moreover, previous studies have suggested that wet deposition dominates SSA removal from the atmosphere (27). Therefore, we focus on the wet deposition (in particular, the below-cloud wet removal as we measured low-altitude SSA).

The rain rate and rain frequency are both positively correlated with the SSA removal rate (31). The ERA5 data during ATom show that the rain rate peaks in the tropics and decreases toward the polar regions, with a smaller peak in the midlatitudes (20 to 60°) for both hemispheres (*SI Appendix*, Fig. S12). This pattern agrees well with the global precipitation products from observations and models (32). The rain scavenging coefficient versus rain rate follows linear log-log relationship for aerosols in the 10^{-3}- to 10-μm size range (31), indicating that a large change in rainfall rate only results in a small change in rainfall scavenging efficiency. Using the formula developed by Andronache (31), we find that the 10 to 18 times higher rain rate in the tropics compared to 80° N latitude (*SI Appendix*, Fig. S12) corresponds to a 4% higher scavenging coefficient in the tropics, suggesting that the scavenging efficiency is nearly independent on latitude. As latitude is a good proxy of SST (*SI Appendix*, Fig. S13*A*), the result indicates that the scavenging efficiency is independent of SST.

The latitudinal distribution of rain frequency is nearly flat from the tropics to almost the polar region, except for a dip in the subtropics (32). We would expect higher SSA concentration in the subtropics if the SSA were strongly influenced by rain frequency. The monotonic decrease of SSA residual from the tropics to the polar regions (*SI Appendix*, Fig. S14) suggests that rain frequency has little influence on the latitudinal distribution of SSA. Nevertheless, we removed data that were associated with greater than 10 $mm \cdot d^{-1}$ rain rate in the previous 24 h or greater than 1 $mm \cdot h^{-1}$ rain rate in the measuring hour (*Materials and Methods*) to minimize the influence of wet removal on the SSA versus SST relationship. Altogether, the analysis suggests little variation of particle wet deposition as a function of latitude and SST. Therefore, the positive correlation of SSA residual with SST suggests that SST enhances SSA production.

Combined Control of SSA Concentration by Wind Speed and SST. The above discussion shows that both wind speed and SST have a positive influence on the production of SSA, with wind speed being the dominant factor. This result is expected as the shear stress of wind on the surface of the water is the fundamental

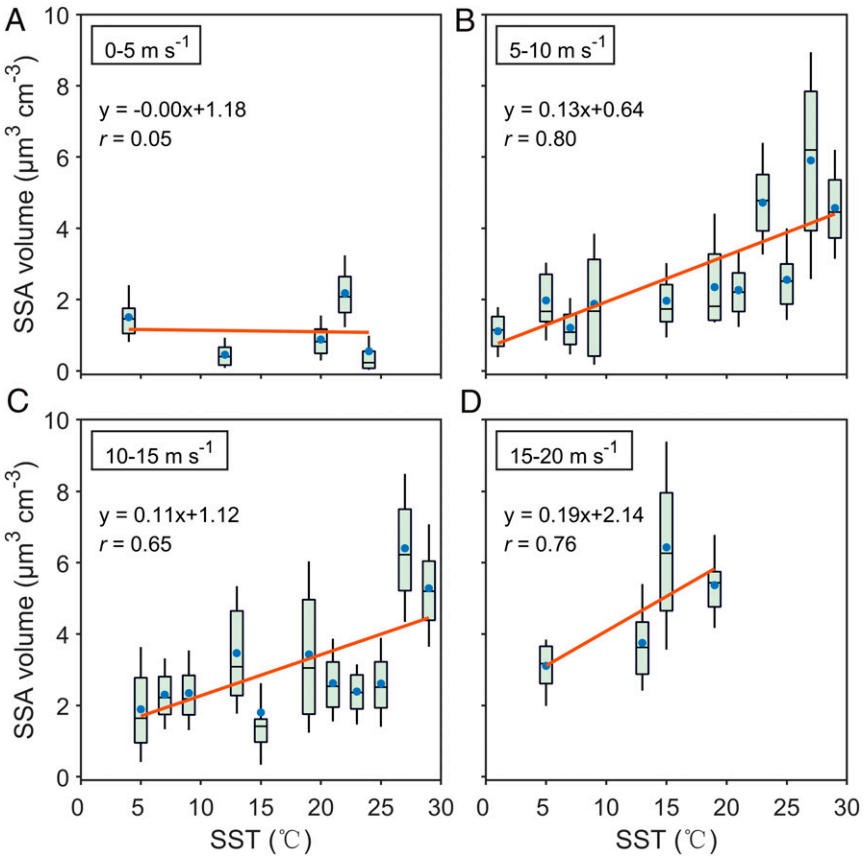

Fig. 4. SSA volume concentration versus SST. SSA volume concentration versus SST for 0 to 5 m · s^{-1} (*A*), 5 to 10 m · s^{-1} (*B*), 10 to 15 m · s^{-1} (*C*), and 15 to 20 m · s^{-1} (*D*) WS_h intervals during ATom2. The definition of the boxes is the same as in Fig. 2*A*. The red line represents the linear regression for the mean values, with the equation and *r* value shown in the legend.

process producing SSA. To examine the synergistic effects of these two factors, we applied the third-order polynomial function to parameterize the measured SSA volume using WS_h and SST (*SI Appendix*, Table S4). Such a method has been used previously (3). The resultant *r* values were significantly ($P < 0.05$) greater than the *r* values for the wind speed or SST alone (*SI Appendix*, Table S5) for all ATom campaigns, demonstrating that using combined wind speed and SST enhances the predictability of SSA.

Conclusions

In summary, our aircraft measurement of aerosol size distributions over global remote oceans provides observational constraints for understanding the formation mechanisms of SSA. Using aerosols of the size range 0.5 to 3 μm as a proxy of SSA, we show that the SSA in the MBL strongly depends on WS_h with a stronger dependence for larger particles, but its concentration is enhanced under higher SST in a wide range of wind speed levels. Furthermore, we show that using wind speed and SST can strengthen the predictability of SSA compared with using wind speed alone. These findings support incorporating SST into global models, which has been shown to substantially reduce model bias against cruise and ground-based measurements. Our aircraft-based global dataset complements the existing database. This advancement offers an opportunity to validate and refine current parameterizations in SSA source functions using wind speed and SST.

Although our observations have extensive latitudinal coverage in both hemispheres, the dataset limits to provide short-duration global averages. Measurements with longer terms in smaller scales are needed to examine the regionally specific seasonal variation of the SSA–SST relationship. The observed greater influence of SST on larger particles at wind speed of 5 to 10 m · s^{-1} requires verification at broader wind speed levels during field studies, and the fundamental principles need to be explored. Despite the demonstrated importance, the effects of SST on SSA are still not understood theoretically. The hypotheses, such as higher SST promotes SSA production by reducing the kinematic viscosity of surface water, are extremely difficult to examine from field observations. Thus, detailed laboratory investigations in controlled environments are critical for a fundamental understanding of SSA abundance and its impacts on climate.

Materials and Methods

The ATom. ATom is one of the NASA Earth Venture Suborbital-2 missions. One major goal of ATom is to investigate the impacts of human activities on atmospheric aerosols (33). Realizing this goal requires a comprehensive understanding of the properties of natural aerosols, from which the anthropogenic effect is measured. In this work, we focus on marine aerosols, which constitute a major fraction of the natural aerosol system, globally (4). During ATom, a suite of aerosol instruments was deployed on the NASA DC-8 aircraft for year-round measurements: July to August 2016 for ATom1, January to February 2017 for ATom2, September to October 2017 for ATom3, and April to May 2018 for ATom4. We obtained measurements from ATom2, ATom3, and ATom4. The aircraft sampled over remote oceans spanning from the Southern Ocean near the South Pole to the Arctic Ocean near the North Pole (*SI Appendix*, Fig. S1). The flight altitude ranged from 150 m to greater than 12 km (*SI Appendix*, Fig. S2), with the majority of the measurements in the MBL taken at the 150- to 200-m (a.s.l.) altitude range. These aircraft measurements provide a rich dataset to study the properties of SSA on a global scale.

Measurements. POPS was deployed onboard the NASA DC-8 aircraft to measure aerosol number size distribution in real-time. POPS is an optical particle counter that measures aerosol particles on a single particle basis (34). The scientific application of POPS has been demonstrated in recent field studies (35). The original design of POPS measures particles with diameters of 0.14 to 3 μm. During ATom, the instrument was modified to enhance the counting statistics of bigger particles by increasing the flow rate from 0.18 $L \cdot min^{-1}$ to 0.75 $L \cdot min^{-1}$. The resulting measurement size range is 0.2 to 5 μm. The POPS-measured particle size was calibrated using size-selected dioctyl sebacate (DOS) (the real part of the refractive index is 1.45) for the size range of 0.2 to 3 μm. Thus, unless specified, the particle diameter reported in this study is DOS-equivalent diameter.

The POPS sampled from a University of Hawaii solid diffuser inlet (36), which has a ≥50% passing efficiency for 5–μm-sized particles. Dry particles were measured during all flights. In addition to POPS, the dry aerosol number size distribution was also measured by an aerosol microphysical properties (AMP) package (37, 38), which consists of a Laser Aerosol Spectrometer, two nucleation-mode aerosol size spectrometers, and two Ultra-High Sensitivity Aerosol Spectrometers. The ambient size distribution was measured using an externally mounted second-generation Cloud, Aerosol, and Precipitation Spectrometer (CAPS [39]). The size ranges of the AMP and CAPS were 0.003 to 4.8 μm and approximate 0.5 to 930 μm, respectively. The AMP sizes were reported as ammonium sulfate-equivalent diameters (real refractive index = 1.53). The CAPS sizes were reported in diameters using a set of refractive indices typical for the measured aerosol type. The flow rate of the AMP is 0.05 $L \cdot min^{-1}$, which is 15 times smaller than the flow rate of POPS. Thus, the POPS measurements were used for analysis in this work because of better counting statistics, especially for bigger particles. The POPS-measured size range accounts for a small fraction (6%) of aerosol number but 84% of aerosol volume (*SI Appendix*, Fig. S15). Therefore, our analysis mainly focuses on aerosol volume, which is proportional to aerosol mass given little variability of aerosol density. Aerosol volume size distribution was converted from number size distribution assuming spherical particles. The original POPS data were averaged to 1-Hz intervals and converted to standard conditions (273.15 K and 1013.25 hPa).

The performance of POPS was evaluated using concurrent measurements by the AMP and CAPS. The DOS-equivalent diameter measured by the POPS was converted to the ammonium sulfate–equivalent diameter for the comparison with AMP. Good agreement of the average vertical profiles by these instruments was achieved from their comparison (*SI Appendix*, Fig. S16).

The flight coordinates and meteorological parameters (horizontal and vertical wind speed, air temperature, and pressure) were measured with the Meteorological Measurement System (MMS). The existence of clouds was reported by the CAPS. The absolute humidity (water vapor mixing ratio) was measured by the Diode Laser Hygrometer (DLH), and the relative humidity (RH) was assessed using the DLH and MMS measurements. Aerosol chemical composition (0.15 to 3 μm) was measured by the PALMS (40). The sea salt particles were identified based on Na^+, K^+, Ca^+, Sr^+, and other chemical signatures in positive polarity mass spectra (40). The sea salt volume was calculated by mapping size-dependent composition measurements from PALMS to the POPS size distribution to produce absolute sea salt volume concentration (40). Four size bins with limits of 0.185, 0.310, 0.514, 1.135, and 3.706 μm were used to derive sea salt volume every 1 min of flight time, as described in Froyd et al. (40). The PALMS–POPS-derived sea salt volume was used in the data screening procedures in the form of volume fraction but was not used in the in-depth data analysis due to the relatively low time and size resolution.

The SST data were obtained from the hourly ERA5 reanalysis datasets with a spatial resolution of 0.25° × 0.25° (https://www.ecmwf.int/en/forecasts/datasets/reanalysis-datasets/era5). We conducted a two-step verification of the SST data. First, we used latitude as a reference, which has been shown to be a good surrogate for SST. SST anti-correlated with latitude with correlation coefficient (r) of 0.97 (*SI Appendix*, Fig. S13*A*). Second, we examined the relationship of SST with water vapor measured by the DLH. SST increased with water vapor (*SI Appendix*, Fig. S13*B*), which is consistent with their expected relationship. Collectively, the evidence suggests that the SST data are of high quality. The ERA5 reanalysis datasets also include the hourly mean wind speed measured at 10 m (a.s.l.) (U_{10}) and the hourly rain rate.

Data Processing. We took the following steps to screen the POPS-measured data for the examination of the SST and SSA relationship. 1) The measurements at the 150- to 200-m (a.s.l.) altitude range were used for data analysis to best represent the surface SSA and winds. 2) Flight measurements over land were excluded (*SI Appendix*, Fig. S1). This procedure also removed data over continental and coastal ice to minimize the influence of sea ice on SSA. However, there might be residual influence by sea ice in the high latitude regions as the ice brine (blowing snow or frost flowers) may transport away from the source region and be measured by our instruments. Since ice brine could be a source of SSA (27, 41), the observed SSA concentration at very low temperatures (~0 °C) would be biased high if the data were affected by sea ice. This indicates that the observed positive relationship of SSA and SST would be stronger if the influence of sea ice were completely eliminated. 3) Since cloud droplets and ice crystals can shatter at the POPS inlet and interfere with the measurement, we removed the cloud-influenced data using the cloud indicator reported from the CAPS measurements. To eliminate the impacts of nonmarine air masses (e.g., air masses from anthropogenic or biomass burning sources), we excluded 4) particles smaller than 0.5 μm, which likely had diverse sources (27), 5) measurements with RH <50%, and 6) measurements with sea salt volume fraction <50%. 7) Finally, we excluded the measurements that were associated with >10 $mm \cdot day^{-1}$ precipitation 24 h prior to the measurement or >1 $mm \cdot h^{-1}$ in the measuring hour to limit the influence of wet deposition.

Step 4 removed 12% of the POPS measurement. Steps 5 through 7 removed 1%, 4%, and 8% of the total data points, respectively. Sensitivity tests suggest that the conclusions were insensitive to steps 4 through 6 because of the small fraction of data removed during these procedures. For step 7, although the results were insensitive to the rain rate of 1 to 10 $mm \cdot day^{-1}$ and 0.2 to 1 $mm \cdot h^{-1}$, we conservatively used the upper bound values to ensure that the data are minimally influenced by precipitation. After screening, the aerosol data should mainly represent SSA.

Measurement Uncertainty. The main source of uncertainty in the POPS measurement is the uncertainty in particle counting. Particle counting statistics follows Poisson distribution (42). Therefore, the uncertainty equals the square root of the particle count. Additional uncertainties include the uncertainties in flow rate (5%) and particle sizing (15%; 34). The overall uncertainty in particle number and volume concentration was 5 to 40% and 45 to 60%, respectively, for the POPS measurement range (0.2 to 3 μm), with larger particles having greater uncertainty. An uncertainty of 16% was derived for the total SSA volume (0.5 to 3 μm), which was the major parameter used for the analysis.

The PALMS particle classification errors are generally estimated at <5% and are likely to be lower in this study since sea salt spectra are very distinctive. The sea salt particle number fraction was averaged over a 3 min sample period. The number fraction reported here does not account for size-dependent biases in PALMS particle detection (40) but nevertheless provides a specific indicator of relative sea salt aerosol abundance. Typical statistical error in SSA volume fraction for the sea salt-rich environments is <3% for SSA ≥ ~1 $\mu g\ stdm^{-3}$ (40). A conservative estimate of uncertainty for the sea salt volume fraction, which also includes about 15% systematic error from simplifying the size distribution, is <20% for the data in this work (40).

Data Availability. Digital data have been deposited in the GitHub Repository, NASA ESPO Data Archive, and ERA5 Reanalysis Data Archive (https://github.com/Chengcheng6/ATom_POPS_data, https://espoarchive.nasa.gov/ and https://www.ecmwf.int/en/forecasts/datasets/reanalysis-datasets/era5).

ACKNOWLEDGMENTS. We acknowledge funding from the NASA ATom project. R.-S.G. was supported by the National Oceanic and Atmospheric Administration (NOAA) Chemical Science Laboratory. S.L. was supported by the NASA Upper Atmospheric Research Program. B.W. and M.D. have received funding from the European Research Council (ERC) under the European Union's Horizon 2020 research and innovation framework program under grant 640458 (A-LIFE) and from the University of Vienna. PALMS was supported by NOAA internal climate funding and also in part by NASA award NNH15AB12I. We thank Charles Brock, Christina Williamson, and Agnieszka Kupc for helping install and operate the POPS instrument and provide the AMP data during the ATom measurements.

1. X. Ma, K. Von Salzen, J. Li, Modelling sea salt aerosol and its direct and indirect effects on climate. *Atmos. Chem. Phys.* **8**, 1311–1327 (2008).
2. M. Z. Jacobson, Global direct radiative forcing due to multicomponent anthropogenic and natural aerosols. *J. Geophys. Res. Atmos.* **106**, 1551–1568 (2001).
3. L. Jaeglé, P. K. Quinn, T. S. Bates, B. Alexander, J.-T. Lin, Global distribution of sea salt aerosols: New constraints from in situ and remote sensing observations. *Atmos. Chem. Phys.* **11**, 3137–3157 (2011).
4. C. D. O'Dowd, G. de Leeuw, Marine aerosol production: A review of the current knowledge. *Philos. Trans. A Math. Phys. Eng. Sci.* **365**, 1753–1774 (2007).
5. H. Grythe, J. Ström, R. Krejci, P. Quinn, A. Stohl, A review of sea-spray aerosol source functions using a large global set of sea salt aerosol concentration measurements. *Atmos. Chem. Phys.* **14**, 1277–1297 (2014).
6. W. K. Melville, P. Matusov, Distribution of breaking waves at the ocean surface. *Nature* **417**, 58–63 (2002).

7. K. A. Prather *et al*., Bringing the ocean into the laboratory to probe the chemical complexity of sea spray aerosol. *Proc. Natl. Acad. Sci. U.S.A.* **110**, 7550–7555 (2013).
8. X. Wang *et al*., The role of jet and film drops in controlling the mixing state of submicron sea spray aerosol particles. *Proc. Natl. Acad. Sci. U.S.A.* **114**, 6978–6983 (2017).
9. L. M. Russell, L. N. Hawkins, A. A. Frossard, P. K. Quinn, T. S. Bates, Carbohydrate-like composition of submicron atmospheric particles and their production from ocean bubble bursting. *Proc. Natl. Acad. Sci. U.S.A.* **107**, 6652–6657 (2010).
10. G. Zheng *et al*., Marine boundary layer aerosol in the eastern North Atlantic: Seasonal variations and key controlling processes. *Atmos. Chem. Phys.* **18**, 17615–17635 (2018).
11. G. de Leeuw *et al*., Production flux of sea spray aerosol. *Rev. Geophys.* **49**, RG2001 (2011).
12. S. D. Forestieri *et al*., Temperature and composition dependence of sea spray aerosol production. *Geophys. Res. Lett.* **45**, 7218–7225 (2018).
13. W. C. Keene *et al*., Factors that modulate properties of primary marine aerosol generated from ambient seawater on ships at sea. *J. Geophys. Res. Atmos.* **122**, 11961–11990 (2017).
14. M. E. Salter, E. D. Nilsson, A. Butcher, M. Bilde, On the seawater temperature dependence of the sea spray aerosol generated by a continuous plunging jet. *J. Geophys. Res. Atmos.* **119**, 9052–9072 (2014).
15. J. Zábori, M. Matisäns, R. Krejci, E. D. Nilsson, J. Ström, Artificial primary marine aerosol production: A laboratory study with varying water temperature, salinity, and succinic acid concentration. *Atmos. Chem. Phys.* **12**, 10709–10724 (2012).
16. M. D. Anguelova, F. Webster, Whitecap coverage from satellite measurements: A first step toward modeling the variability of oceanic whitecaps. *J. Geophys. Res. Oceans* **111**, C03017 (2006).
17. E. R. Lewis, S. E. Schwartz, *Sea Salt Aerosol Production: Mechanisms, Methods, Measurements, and Models–A Critical Review* (American Geophysical Union, Washington, DC, 2004).
18. T. Dror, Y. Lehahn, O. Altaratz, I. Koren, Temporal-scale analysis of environmental controls on sea spray aerosol production over the South Pacific Gyre. *Geophys. Res. Lett.* **45**, 8637–8646 (2018).
19. S. Christiansen, M. E. Salter, E. Gorokhova, Q. T. Nguyen, M. Bilde, Sea spray aerosol formation: Laboratory results on the role of air entrainment, water temperature, and phytoplankton biomass. *Environ. Sci. Technol.* **53**, 13107–13116 (2019).
20. Y. Lehahn *et al*., Decoupling atmospheric and oceanic factors affecting aerosol loading over a cluster of mesoscale North Atlantic eddies. *Geophys. Res. Lett.* **41**, 4075–4081 (2014).
21. E. M. Mårtensson, E. D. Nilsson, G. de Leeuw, L. H. Cohen, H.-C. Hansson, Laboratory simulations and parameterization of the primary marine aerosol production. *J. Geophys. Res. Atmos.* **108**, 4297 (2003).
22. M. E. Salter *et al*., An empirically derived inorganic sea spray source function incorporating sea surface temperature. *Atmos. Chem. Phys.* **15**, 11047–11066 (2015).
23. A. N. Schwier *et al*., Primary marine aerosol physical flux and chemical composition during a nutrient enrichment experiment in mesocosms in the Mediterranean Sea. *Atmos. Chem. Phys.* **17**, 14645–14660 (2017).
24. G. Saliba *et al*., Factors driving the seasonal and hourly variability of sea-spray aerosol number in the North Atlantic. *Proc. Natl. Acad. Sci. U.S.A.* **116**, 20309–20314 (2019).
25. J. Ovadnevaite *et al*., A sea spray aerosol flux parameterization encapsulating wave state. *Atmos. Chem. Phys.* **14**, 1837–1852 (2014).
26. S. Barthel, I. Tegen, R. Wolke, Do new sea spray aerosol source functions improve the results of a regional aerosol model? *Atmos. Environ.* **198**, 265–278 (2019).
27. D. M. Murphy *et al*., The distribution of sea-salt aerosol in the global troposphere. *Atmos. Chem. Phys.* **19**, 4093–4104 (2019).
28. P. K. Quinn, D. J. Coffman, J. E. Johnson, L. M. Upchurch, T. S. Bates, Small fraction of marine cloud condensation nuclei made up of sea spray aerosol. *Nat. Geosci.* **10**, 674 (2017).
29. M. Motta, R. J. Barthelmie, P. Vølund, The influence of non-logarithmic wind speed profiles on potential power output at Danish offshore sites. *Wind Energy (Chichester Engl.)* **8**, 219–236 (2005).
30. M. L. Witek, P. J. Flatau, J. Teixeira, K. M. Markowicz, Numerical investigation of sea salt aerosol size bin partitioning in global transport models: Implications for mass budget and optical depth. *Aerosol Sci. Technol.* **45**, 401–414 (2011).
31. C. Andronache, Estimated variability of below-cloud aerosol removal by rainfall for observed aerosol size distributions. *Atmos. Chem. Phys.* **3**, 131–143 (2003).
32. R. F. Adler, C. Kidd, G. Petty, M. Morissey, H. M. Goodman, Intercomparison of global precipitation products: The third Precipitation Intercomparison Project (PIP-3). *Bull. Am. Meteorol. Soc.* **82**, 1377–1396 (2001).
33. M. J. Prather *et al*., Global atmospheric chemistry–Which air matters. *Atmos. Chem. Phys.* **17**, 9081–9102 (2017).
34. R. S. Gao *et al*., A light-weight, high-sensitivity particle spectrometer for PM2.5 aerosol measurements. *Aerosol Sci. Technol.* **50**, 88–99 (2016).
35. Y. Y. Cui *et al*., Religious burning as a potential major source of atmospheric fine aerosols in summertime Lhasa on the Tibetan Plateau. *Atmos. Environ.* **181**, 186–191 (2018).
36. C. S. McNaughton *et al*., Results from the DC-8 Inlet Characterization Experiment (DICE): Airborne versus surface sampling of mineral dust and sea salt aerosols. *Aerosol Sci. Technol.* **41**, 136–159 (2007).
37. C. A. Brock *et al*., Aerosol size distributions during the atmospheric Tomography mission (ATom): Methods, uncertainties, and data products. *Atmos. Meas. Tech.* **12**, 3081–3099 (2019).
38. C. A. Brock *et al*., Aerosol optical properties in the southeastern United States in summer–Part 1: Hygroscopic growth. *Atmos. Chem. Phys.* **16**, 4987–5007 (2016).
39. A. Spanu, M. Dollner, J. Gasteiger, T. Paul Bui, B. Weinzierl, Flow-induced errors in airborne in situ measurements of aerosols and clouds. *Atmos. Meas. Tech.* **13**, 1963–1987 (2020).
40. K. D. Froyd *et al*., A new method to quantify mineral dust and other aerosol species from aircraft platforms using single-particle mass spectrometry. *Atmos. Meas. Tech.* **12**, 6209–6239 (2019).
41. J. Huang, L. Jaeglé, Wintertime enhancements of sea salt aerosol in polar regions consistent with a sea ice source from blowing snow. *Atmos. Chem. Phys.* **17**, 3699–3712 (2017).
42. G. Buonanno, M. Dell'Isola, L. Stabile, A. Viola, Uncertainty budget of the SMPS-APS system in the measurement of PM1, PM2.5, and PM10. *Aerosol Sci. Technol.* **43**, 1130–1141 (2009).